PAPER

Check for updates

Efficient and sustainable hydrogen evolution reaction: enhanced photoelectrochemical performance of ReO₃-incorporated Cu₂Te catalysts†

Aruna Vijayan and N. Sandhyarani ⓘ D *

In the pursuit of clean hydrogen production, the photoelectrochemical hydrogen evolution reaction (HER) plays a pivotal role. The development of highly efficient, durable catalysts is vital for the industrialization of water-splitting technology. One promising strategy is the fabrication of self-supported catalysts, which are known for their exceptional activity and durability. In this study, we report the synthesis of copper telluride (Cu₂Te) incorporated with rhenium oxide (ReO₃) *via* a CVD-assisted route. The electrochemical and photoelectrochemical HER performance analyses reveal that the ReO₃–Cu₂Te composite exhibits excellent HER performance with a very low overpotential of -0.026 V at -10 mA cm^{-2} in the presence of light. This exceptional performance positions the ReO₃–Cu₂Te composite as a promising candidate to replace the expensive state-of-the-art platinum catalyst.

1. Introduction

The world's energy demands contribute to the transition to an era beyond fossil fuels. Green hydrogen production by water splitting is a promising and sustainable energy production method. To deploy water splitting as a commercial method for the production of hydrogen, the catalyst should possess certain merits such as earth abundance, compatibility, scalability, and low fabrication cost.[1] To date, platinum has been considered the most efficient catalyst for the hydrogen evolution reaction.[2] Low earth abundance and high cost prevent platinum from being used for large-scale industrial applications. Dedicated research is being carried out to develop an efficient, inexpensive, and stable alternative to platinum.

Transition metal chalcogenides (TMCs),[3] nitrides,[4] oxides,[5] and phosphides[6] are some of the active catalytic materials recently reported for the hydrogen evolution reaction (HER). The low cost of the constituent elements, good electrocatalytic activity, the existence of various polymorphs, tunable band gaps, and metallic properties upon thinning are some of the peculiar properties of TMCs.[7] Among TMCs, copper chalcogenides find applications in thermoelectric generators, photodetectors, light emitting diodes, solar cells, and photocatalysis,

owing to their various structural forms and fascinating physical properties.[8,9] The literature points out the advantage of Cu, owing to its high d electron occupancy.[10] Compared to Fe, Co, and Ni, Cu is suitable for energy storage and conversion applications due to its excellent electrical conductivity, favorable stability, and cost-effectiveness.[11] However, copper chalcogenides are rarely reported compared to molybdenum,[12] nickel,[13] cobalt,[14] and tungsten chalcogenides[14] for the HER. Among different copper chalcogenides, copper telluride has attracted recent research interest due to its ultralow thermal conductivity and superionic conductivity.[9] Tellurium is less electronegative and heavier than other chalcogenides. Reports show that the catalytic performance of metal-based catalysts can be enhanced by increasing the covalent character of the metal–anion bond. Among the chalcogenides, tellurium has less electronegativity compared to sulfur and selenium, resulting in stronger metal–telluride (M–Te) bonds with increased covalent character. This increased covalency of M–Te bonds lowers the reduction potential of metals facilitating the generation of catalytically active sites.[15] Also among different transition metal chalcogenides, transition metal tellurides have quasi-metallic properties and hence exhibit superior conductivity and mass transport rate. Compared to sulfide and selenide derivatives, copper telluride is less explored.

Transition metal oxides (TMOs) are another class of widely studied photo-, electro-, and photo-electrocatalysts towards the hydrogen evolution reaction. The TMOs generally suffer from fast charge carrier recombination, affecting their photo/photoelectrocatalytic activity. Several methods are reported to alleviate the fast recombination. TMOs with oxygen vacancies are considered prospective materials to increase the catalytic activity of a

Nanoscience Research Laboratory, Department of Materials Science and Engineering, National Institute of Technology Calicut, Calicut, Kerala, India. E-mail: sandhya@nitc.ac.in

catalyst,[16] and help to tune the bandgap and provide more active sites and have favorable Gibbs hydrogen adsorption free energies.[17] Formation of heterostructures is another means to decrease the charge recombination and increase the photo-catalytic efficiency.[16] Formation of a heterostructure of TMO and TMC with appropriate band gap alignment is a potential method to improve the HER, which is addressed in this work.

Among different elements, rhenium is at the forefront as an HER catalyst, exhibiting optimal binding energy for adsorption and desorption of protons and an excellent exchange current density comparable to platinum. Re has great potential to replace Pt, but more studies are needed in this regard.[18,19] Owing to its different valence states, rhenium oxide finds great potential in technological and industrial applications such as fuel cells, heterogeneous catalysis, etc[20,21] Reports suggest that ReO_3 exhibits localized surface plasmon resonance (LSPR) in the visible region similar to gold nanoparticles or metallic copper due to the available free electrons in the conduction band and the partially filled conduction band.[22] So far, very limited studies have been conducted on the HER properties of ReO_3.

Although a variety of TMC and TMO-based catalysts have been synthesized, most of them are in powder form. A powder catalyst often requires a binder to be cast on a substrate for electrochemical testing. This increases the interfacial resistance between the catalyst and electrolyte, blocks the active site of the catalyst, and results in reduced HER activity.[23] Deposition of a catalyst on a conductive substrate is a promising strategy, which often provides nano- or microstructures with a large number of active edge sites and lower diffusion lengths for charge and mass transport.[24] Cu foam (CuF) can be used for materials growth, and its low cost and high electrical conductivity make it suitable as an electrode substrate.[25] Typically, self-supported catalysts can be synthesized by different synthesis approaches such as electrodeposition, hydro/solvothermal synthesis, freeze drying, vacuum filtration, physical/chemical vapor deposition, $etc.$ Among these different methods, chemical vapor deposition (CVD) yields 2D materials of high quality and high yield.[26] The literature reports the enhanced activity of chemical vapor deposited TMDs owing to their more exposed active edge sites.[27]

The present work establishes a strategy for designing a self-supported catalyst by chemical vapor deposition using Cu foam as the substrate and the precursor for the formation of copper telluride. This ensures the strong interaction between the active materials and the substrate, enhancing its activity toward the HER. By incorporating ReO_3 into Cu_2Te, the HER activity of copper telluride is enhanced significantly. The synthesized ReO_3–Cu_2Te catalyst exhibited a lower overpotential of -0.026 V at -10 mA cm^{-2} in the presence of light. Such a lower overpotential underlines its competence with Pt catalysts.

2. Experimental methods

2.1. Materials

Ammonium perrhenate ($\geq$99%) and tellurium powder (99.8%, 200 mesh) were procured from Sigma Aldrich.

2.2. Synthesis of copper telluride incorporated with rhenium oxide

Chemical vapor-deposition-assisted synthesis was carried out to prepare a copper telluride–rhenium oxide composite. For the synthesis, tellurium powder and ammonium perrhenate were used as precursors. The schematic representation of the synthesis is given in Scheme 1. 250 mg of tellurium powder was taken in an alumina boat and placed in zone 2 of the quartz tube furnace, where the temperature was ramped up to 650 °C. 50 mg of ammonium perrhenate taken in an alumina boat was placed in zone 1, where the temperature was ramped up to 500 °C. Cu foam of 1 cm^2 × 2 cm^2 dimensions was also placed on top of the same alumina boat. Prior to ramping up the temperature, argon gas was purged through the furnace at a flow rate of 150 sccm for 15 min. The two different zones of the furnace were then ramped up to 500 °C and 650 °C in 30 minutes and then kept at 500 °C and 650 °C for 30 min with a constant flow rate of argon gas at 150 sccm under atmospheric pressure. The furnace was then turned off and allowed to cool to 35 °C. To investigate the electrochemical and photo-electrochemical HER properties of other copper chalcogenides upon ReO_3 incorporation, the same synthesis process was repeated with S and Se powders instead of tellurium powder.

3. Results and discussion

3.1. Morphological characterization

Morphological analysis of ReO_3–Cu_2Te was carried out using FE-SEM, which revealed the growth of the catalyst on the surface of the copper foam. The SEM images of the ReO_3–Cu_2Te composite at different magnifications are given in Fig. 1(a) and (b), which show thick flake-like deposits. The morphological distinction between ReO_3 and Cu_2Te is not possible from these SEM images. To investigate the presence of the elements, energy dispersive spectroscopy (EDS) analysis was carried out. The presence of copper, tellurium, rhenium, and oxygen was proven using the EDS spectrum (Fig. 1(c)) and the EDS mapping (Fig. 1(e)–(i)).

3.2. Chemical characterization

The crystallinity of copper telluride incorporated with rhenium oxide was analysed using XRD, which is shown in Fig. 2(a). The composite exhibits strong peaks at 43.5°, 50.4°, and 73.9° corresponding to (111), (200), and (220) planes of the cubic crystal system of copper (00-003-1005), which arise from the Cu
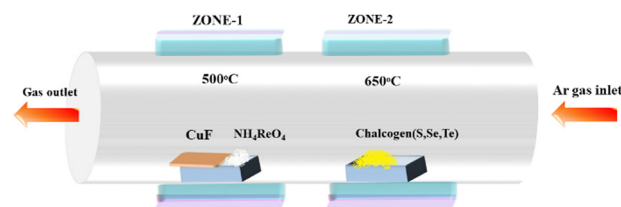
Scheme 1 Schematic representation of chemical vapor deposition of copper chalcogenides incorporated with rhenium oxide.
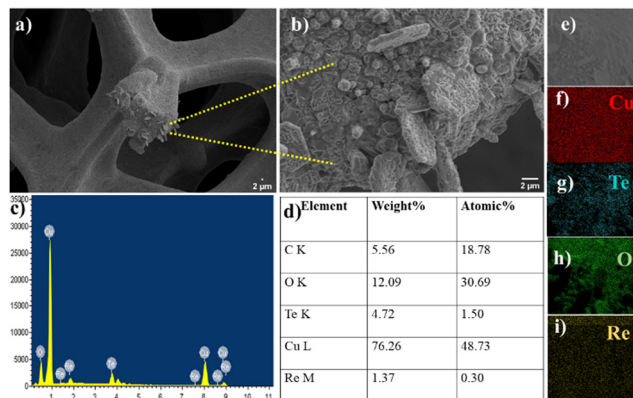
Fig. 1 (a) and (b) SEM image and magnified SEM image of ReO₃–Cu₂Te. (c) EDS spectrum of ReO₃–Cu₂Te. (d) Elemental composition of ReO₃–Cu₂Te. (e)–(i) Elemental mapping of Cu, Te, O, and Re.

foam. The diffractions at 12.1°, 24.3°, 27.1°, 42.2°, and 44.6° correspond to the planes (001), (002), (101), (110), (103) of Cu_2Te (03-065-3460) with hexagonal structure. As evident from the EDS analysis, the concentration of rhenium oxide is very low in the composites. To identify in which form rhenium was incorporated in the materials, ammonium perrhenate alone was treated under the same synthesis conditions in the absence of Cu. The XRD analysis of the material suggests the formation of rhombohedral ReO_3 (00-045-1039) along with traces of monoclinic ReO_2 (00-017-0600), which is shown in Fig. S2 (ESI†). In the ReO_3–Cu_2Te (Fig. 2(a)) composite, the peaks observed at 24.3°, 42.2°, and 61.5° correspond to the planes (200), (222), and (422) of ReO_3 (03-065-4073) belonging to the cubic crystal structure. Upon composite formation, ReO_3 exhibited a phase transition. Rhenium trioxide has a perovskite-type (ABO_3) structure composed of a regular octahedron joined by vertices with an unoccupied perovskite A site.[28] When these metal centers are linked by a ligand, coordination polymers form. It has been reported that such copolymers exhibit structural phase transition induced by the order–disorder motion of the ligand.[29] Cu foam is prone to oxidation upon exposure to air. The peaks at 36°, 41.7°, 61.2°, and 73.9° correspond to (111), (200), (220) and (311) planes of Cu_2O (01-078-2076). It is not considered as a distinct component in this manuscript, since its presence is inevitable even in bare
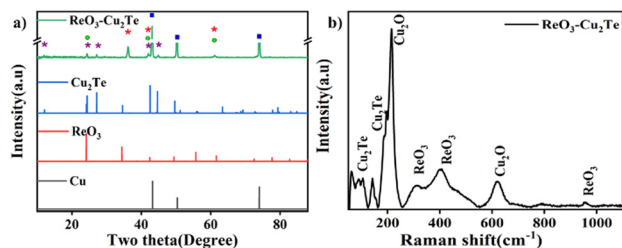
copper foam. The reported electrochemical HER value of bare copper foam (CuF) includes the performance of Cu_2O.

Raman spectrum of ReO_3–Cu_2Te is shown in Fig. 2(b). The material exhibits strong peaks at around 217 cm⁻¹ and 620 cm⁻¹ arising from the second overtone mode and Raman forbidden first order mode of Cu_2O, which are due to the oxidation of the base material Cu foam.[30] The peak at 140 cm⁻¹ corresponds to the A_{1g} vibrational mode of Cu–Te.[31] The peak at 105 cm⁻¹ also supports the existence of Cu_2Te.[32] The peaks around 325 cm⁻¹ and 950 cm⁻¹ correspond to the Re–O stretching vibration of ReO_3.[33] A broad peak at 400–500 cm⁻¹ arises due to the presence of ReO_3.[34,35]

XPS analysis was carried out to identify the chemical state associated with each element. All the values reported here are carbon corrected to the C 1s peak at 284.7 eV. The survey spectrum of ReO_3–Cu_2Te given in Fig. 3(a) reveals the presence of Cu, Te, Re, and O in the material. The peaks at 933.04 eV and 952.92 eV are assigned to the Cu $2p_{3/2}$ and Cu $2p_{1/2}$ peaks of the Cu^{1+} state.[36] The core level spectrum of tellurium (Fig. 3(c)) exhibits a peak at binding energies 573.6 eV and 583.72 eV corresponding to the Te $3d_{5/2}$ and Te $3d_{3/2}$ of the Te^{2-} state.[37] Along with the peaks corresponding to Te, the Cu LLM peak at 570.17 eV and 575.1 eV, which arises from the Cu foam, was observed.[38] The peak of Re at 46.25 eV and 48.59 eV represents the oxidized rhenium with a +6 oxidation state along with traces of a +4 oxidation state.[39] The high-resolution oxygen spectrum shows two peaks at binding energies 530.95 eV and 532.11 eV. This indicates that there are two types of oxygen present in the material. One from the oxides of rhenium and another from the oxygen vacancies of the material.[40]

Usually, the O 1s spectrum can be resolved into three peaks. The peak at 529.5 ± 0.4 eV corresponds to lattice oxygen, the peak at 531.2 ± 0.6 eV corresponds to oxygen-deficient regions, and the peak at 532.5 ± 0.5 due to loosely bound oxygen on the surface such as in H_2O and OH groups.[41] The high energy peak is absent for ReO_3–Cu_2Te, since the XPS spectrum is taken after etching. Thermal treatment during CVD synthesis of ReO_3–Cu_2Te helps to create oxygen vacancies. Electrochemical and photoelectrochemical HER results indicate that these oxygen vacancies help enhance the catalytic activity of the catalyst.
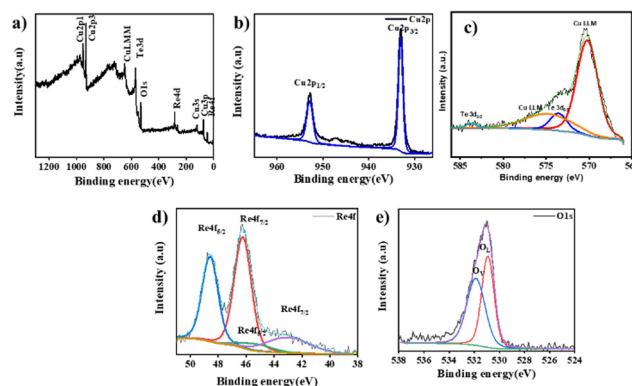

Fig. 2 (a) XRD pattern of ReO₃–Cu₂Te, in the XRD pattern, ■, *, ●, and * represent Cu, Cu₂Te, ReO₃, and Cu₂O, respectively. (b) Raman spectrum of ReO₃–Cu₂Te.

Fig. 3 Survey spectrum of (a) ReO₃–Cu₂Te. Elemental spectra of (b) Cu 2p, (c) Te 3d, (d) Re 4f, and (e) O 1s of ReO₃–Cu₂Te.

© 2024 The Author(s). Published by the Royal Society of Chemistry

As mentioned above, Cu_2O is present even with bare copper foam. Oxygen vacancies can also arise from Cu_2O. However, the electrochemical HER performance (Section 3.3) of the copper chalcogenide and ReO_3 incorporated copper chalcogenides demonstrates the beneficial effect of the incorporation of ReO_3. Copper chalcogenide alone, wherein Cu_2O is present, does not show a similar activity enhancement. This led to the conclusion that oxygen vacancies are created during ReO_3 incorporation.

In order to investigate the presence of oxygen vacancies EPR spectroscopy[42] was carried out for ReO_3–Cu_2Te and the spectrum is given in Fig. S3 (ESI†). The EPR spectrum of ReO_3–Cu_2Te shows an intense EPR signal at a *g* value of 2.15, indicating the presence of oxygen vacancies in the material.[43]

3.3. Electrochemical hydrogen evolution reaction

To assess the electrochemical HER performance of the catalyst, the linear sweep voltammetry technique was used. The polarization curves of CuF, Cu_2Te, and ReO_3–Cu_2Te are shown in Fig. 4(a). The potential values obtained with Ag/AgCl were calibrated to the reversible hydrogen electrode (RHE). The details of the calibration experiment are given in the ESI† (Fig. S1). Cu_2Te exhibits an overpotential of -0.34 V, at -10 mA cm^{-2}. When rhenium oxide was introduced, the overpotential of ReO_3–Cu_2Te was decreased to -0.07 V, at -10 mA cm^{-2}. The very low overpotential of ReO_3–Cu_2Te proves that the rhenium oxide–copper chalcogenide catalyst can be a promising substitute for Pt catalysts. Other chalcogenides, such as Cu_2S and Cu_2Se, incorporated with ReO_3 were synthesized using a similar synthesis method. Their electrochemical HER analyses are given in Fig. S4 (ESI†). It is found that among different ReO_3-incorporated copper chalcogenides, ReO_3–Cu_2Te exhibits lower overpotential and higher current density.

3.4. Stability

The chemical robustness of a catalyst is of critical importance when it comes to industrial applications. The accelerated durability test (ADT) of ReO_3–Cu_2Te was performed in 0.5 M H_2SO_4 using chronoamperometry for 20 000 seconds. Fig. 4(b) shows the current density as a function of time. The *i*–*t* amperometry study was performed at a constant potential of -0.3 V with a sample interval of 0.1 s. The initial surge in current can be due to charging current. A similar trend in the current for long term operation confirms that the ReO_3–Cu_2Te

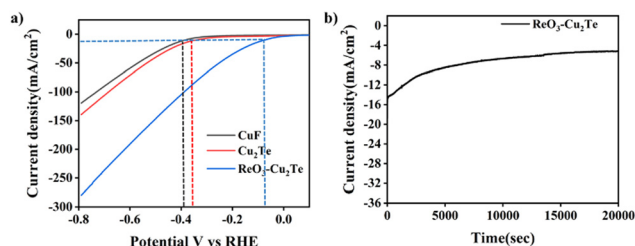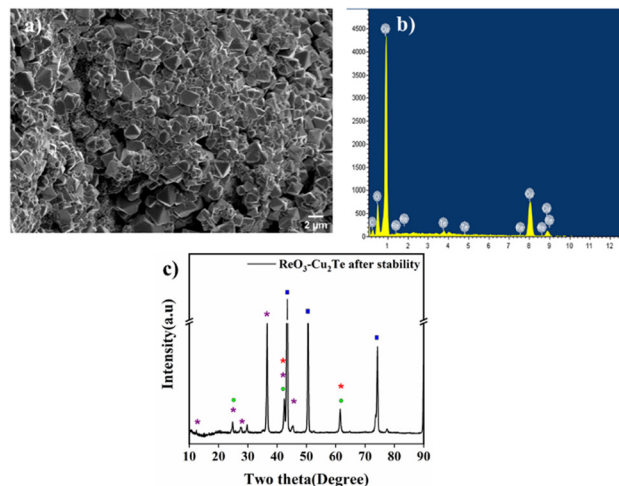**Fig. 5** (a) SEM image, (b) EDS spectrum, and (c) XRD pattern of ReO_3–Cu_2Te after the stability test. In the XRD pattern, ■, *, ●, and * represent Cu, Cu_2Te, ReO_3, and Cu_2O respectively.

catalyst exhibits good stability. ReO_3–Cu_2Te exhibits a current density change of only ~ 9 mA cm^{-2} during the *i*–*t* amperometric durability analysis.

FE-SEM and XRD analyses were performed to identify the morphological and chemical changes that occurred during the durability test (Fig. 5). Cu_2Te–ReO_3 appears as small flakes after the stability test. All the flakes appeared as small polyhedron like deposits. The presence of all the elements after ADT was confirmed by EDS analysis. This confirms that no leaching occurs during the test. After ADT, the catalysts were analyzed using XRD to identify structural characteristics (Fig. 5(c)). ReO_3–Cu_2Te after the stability test exhibits peaks at 24.5°, 42.2°, and 61.5°, which correspond to (200), (222), and (422) planes of ReO_3 in the cubic phase. The peaks at 12.2°, 24.6°, 27.7°, 36.5°, 42.3°, and 44.9° represent (001), (002), (101), (003), (110), and (103) planes of hexagonal Cu_2Te. Apart from the diffractions of the composite, peaks at 43.2°, 50.5°, and 73.9° corresponding to the planes (111), (200), and (220) of cubic Cu are observed. Along with these peaks, as mentioned in Section 3.2, copper oxide (Cu_2O) peaks are also present.

3.5. Photoelectrochemical hydrogen evolution reaction

CVD synthesized photocathodes were utilized to study the photoelectrochemical HER activity. For this study, a 250 W halogen light source with visible-range absorption was used. The electrolyte used was 0.5 M H_2SO_4. Fig. 6(a) presents the photoelectrochemical polarisation curves of different copper chalcogenides incorporated with rhenium oxide. The results suggest that Cu_2Te exhibits higher HER activity in the presence of light than under dark conditions. Upon incorporation of ReO_3, the heterostructure followed this trend. ReO_3–Cu_2Te under dark conditions exhibits an overpotential of -0.074 V, and under light irradiation, it exhibits a lower overpotential of -0.026 V. ReO_3–Cu_2Te exhibits a change in current density of ~ 18 mA cm^{-2} upon light irradiation. The presence of oxygen vacancies in ReO_3 enhances the photoactivity of the catalyst.[44]
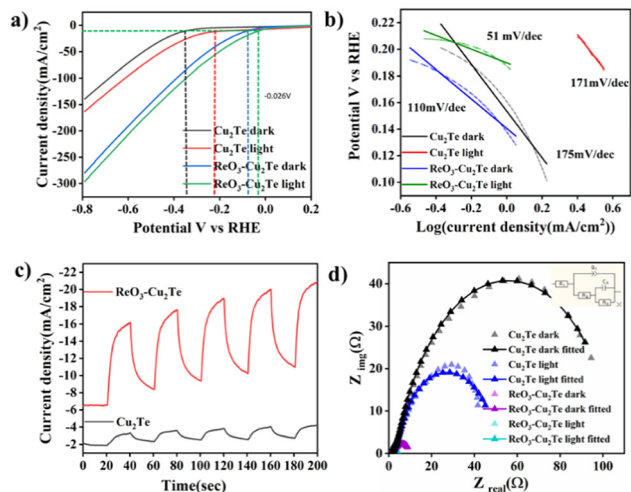

Fig. 4 (a) Polarisation curve of CuF, Cu_2Te, and ReO_3–Cu_2Te. (b) *i*–*t* amperometry curve of ReO_3–Cu_2Te.

Fig. 6 (a) Polarisation curve of Cu_2Te and ReO_3–Cu_2Te under dark conditions and under light-irradiation. (b) Tafel slope of Cu_2Te and ReO_3–Cu_2Te under dark conditions and under light-irradiation. (c) Chronoamperometry curve of Cu_2Te and ReO_3–Cu_2Te. (d) Nyquist plot of Cu_2Te and ReO_3–Cu_2Te under dark conditions and light-irradiation with the corresponding equivalent circuit.

Photoelectrochemical HER analysis carried out for copper sulfide and copper selenide incorporated with ReO_3 is given in Fig. S5 (ESI†). Among different ReO_3-incorporated copper chalcogenides ReO_3–Cu_2Te exhibits the lowest overpotential under light irradiation.

The Tafel slope values were calculated to understand the mechanism of the reaction (Fig. 6(b)). Tafel plots were generated from LSV, and from the linear region of Tafel plots, Tafel slopes were calculated. ReO_3–Cu_2Te exhibited a Tafel slope of 51 mV dec^{-1}, upon light irradiation. Tafel slope analysis suggests that the catalytic process involves a Volmer–Tafel mechanism in which the recombination of adsorbed hydrogen atoms is the rate-determining step. The smaller Tafel slope value of this composite compared to Cu_2Te indicates enhanced HER activity of the composite.

The photocurrent of the catalyst is studied by chronoamperometry, which is shown in Fig. 6(c). Intermittent light illumination at an interval of 20 s was carried out at a constant potential of −0.3 V with a sample interval of 0.1 s. As depicted in Fig. 6(c), rhenium oxide incorporation increases the photocurrent density of copper telluride. The enhanced photocurrent density is direct evidence of the enhanced electron availability upon light irradiation.

A detailed analysis of the charge transfer mechanism was studied using electrochemical impedance spectroscopy (EIS). By keeping the potential constant at −0.3 V vs. Ag/AgCl, EIS studies were performed in 0.5 M H_2SO_4 from a high frequency of 10^5 Hz to a low frequency of 0.08 Hz. The Nyquist plot obtained after fitting along with the equivalent circuit is given in Fig. 6(d). The equivalent circuit consists of solution resistance R_1, charge transfer resistance R_3, constant phase element Q_1, and capacitance C_3. The additional resistance component R_2 in the equivalent circuit indicates that the electrochemical
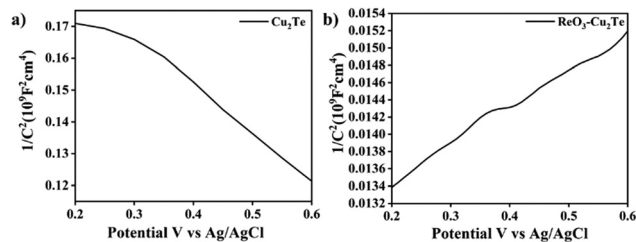

Fig. 7 The Mott–Schottky plots of (a) Cu_2Te and (b) ReO_3–Cu_2Te.

reaction involves the adsorption of the reaction intermediate. Cu_2Te under dark conditions exhibits a higher charge transfer resistance (102.8 Ω). In the presence of light charge transfer resistance decreases to 33.93 Ω. The composite ReO_3–Cu_2Te exhibited a much lower charge transfer resistance of 8.899 Ω under dark conditions. Under light irradiation, the charge transfer resistance of the composite was further reduced to 1.278 Ω. This trend observed for the composite demonstrates the benefit of ReO_3 incorporation for the photoexcitation, charge separation, and transport of the composite, illustrating enhanced electrical conductance. The fitted circuit parameter values are given in Table S1 (ESI†).

The Mott–Schottky (M–S) analysis gives an insight into the charge carriers in the photoelectrodes. Before ReO_3 incorporation, the Mott–Schottky plot of Cu_2Te exhibited a negative slope, which suggests the p-type behavior of the semiconductors, where the major charge carriers are holes. This is consistent with the literature. However, after the incorporation of ReO_3, ReO_3–Cu_2Te showed a positive slope and behaved as an n-type (Fig. 7) semiconductor with electrons as the major charge carriers.

The band gap of the catalyst was estimated by UV-vis diffuse reflectance spectroscopy. Fig. S6 (ESI†) presents the UV-vis diffuse reflectance spectra of Cu_2Te and ReO_3 incorporated Cu_2Te. The energy gap for the direct allowed transitions was determined using the Tauc plot (Fig. S6b and c, ESI†). Cu_2Te shows absorption in the visible region, which is retained after the incorporation of rhenium oxide. The bandgap of the materials was calculated using the Tauc plot. Cu_2Te exhibited a bandgap of 1.61 eV. Upon incorporating ReO_3 its bandgap reduced to 1.47 eV.

3.6. Proposed mechanism

On account of the above results and band edge positions of copper telluride and rhenium oxides a plausible mechanism for the photoelectrochemical behavior of the composite is suggested as follows: generally, upon composite formation, the beneficial arrangement of band position facilitates improved light absorption and efficient charge separation. In such cases, upon contact, the Fermi level of semiconductors equilibrates, and an internal electric field is generated. This internal electric field promotes the electron movement from the conduction band (CB) of Cu_2Te to the CB of ReO_3, which in turn, increases the lifetime of the electron–hole pair. These electrons are then utilized for the reduction of H^+ ions into H_2. In addition to the
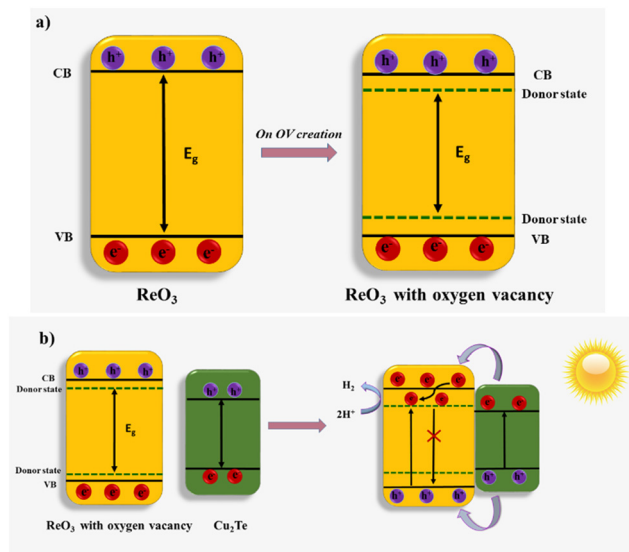
Fig. 8 (a) Schematic illustration of the energy band structure and (b) the proposed photocatalytic mechanism of the Cu_2Te–ReO_3 composite.

above-mentioned mechanism, oxygen vacancies also play a role in tuning the bandgap, extending the absorption range and charge carrier separation leading to an overall enhancement of the photoelectrochemical reaction of the composite. Localized electrons trapped in these vacancies are injected into the adjacent empty 3d orbital of metal atoms. This will create a donor level below the conduction band minimum (CBM). The unsaturated metal atom also participates in electron donation to the oxygen atom that surrounds the defective site. This creates another donor level above the valence band maximum (VBM).[44] Formation of these two donor states effectively helps to reduce the bandgap of ReO_3. This bandgap tuning is illustrated in Fig. 8(a). The donor state below the CBM acts like an intermediate energy level and harvests photons with lower energy. Moreover, these oxygen vacancy states trap the electrons that participate in the subsequent HER reaction. Thus, rhenium oxide incorporated copper telluride benefits from both heterostructure formation and the oxygen vacancy creation on ReO_3, which effectively contribute towards the catalytic activity. This mechanism is given in Fig. 8(b).

4. Conclusion

In summary, the present work established a CVD-synthesized rhenium oxide–copper chalcogenide composite as an efficient electro- and photo-electrocatalyst for the hydrogen evolution reaction. The electrochemical and photoelectrochemical performances of self-supported rhenium oxide incorporated Cu_2Te were analyzed using linear sweep voltammetry, chronoamperometry, electrochemical impedance spectroscopy, Mott–Schottky analysis, *etc.*, which confirmed the enhanced performance after rhenium oxide incorporation. The ReO_3–Cu_2Te composite exhibited the highest HER performance with a very low overpotential of −0.026 V at −10 mA cm^{-2} in the presence of light,

confirming that this combination is a promising candidate to replace the costly platinum catalyst. The oxygen vacancies created during the incorporation of ReO_3 through the CVD synthesis help enhance the catalytic properties. The work provided future insight into the wide opportunity of utilizing ReO_3 and its combination with different TMDs for efficient energy conversion and storage applications.

Conflicts of interest

The authors declare no competing financial interest.

Acknowledgements

Notes and references

1 Y.-X. Yu, L. Pan, M.-K. Son, M. T. Mayer, W.-D. Zhang, A. Hagfeldt, J. Luo and M. Grätzel, *ACS Energy Lett.*, 2018, **3**, 760–766.

2 M. B. Askari and P. Salarizadeh, *Synth. Met.*, 2019, **256**, 116131.

3 H. Su, X. Pan, S. Li, H. Zhang and R. Zou, *Carbon Energy*, 2023, **8**, 1851–1863.

4 J. Theerthagiri, S. J. Lee, A. P. Murthy, J. Madhavan and M. Y. Choi, *Curr. Opin. Solid State Mater. Sci.*, 2020, **24**, 100805.

5 Y. Zhang, W. Liao and G. Zhang, *J. Power Sources*, 2021, **512**, 230514.

6 K. Bhunia, M. Chandra, S. Kumar Sharma, D. Pradhan and S.-J. Kim, *Coord. Chem. Rev.*, 2023, **478**, 214956.

7 J. Yang and H. S. Shin, *J. Mater. Chem. A*, 2014, **2**, 5979–5985.

8 X.-W. Lv, Q.-H. Kong, X.-L. Song, Y.-P. Liu and Z.-Y. Yuan, *Inorg. Chem. Front.*, 2022, **9**, 6182–6189.

9 Y. Zhang, Z. Zhang, W. Liu, Y. Zheng, Y. Wu, J. Su, N. Liu and Y. Gao, *J. Mater. Chem. A*, 2021, **9**, 26095–26104.

10 T. Li, Q. Zhang, X. H. Wang, J. Luo, L. Shen, H. C. Fu, F. Gu, N. B. Li and H. Q. Luo, *Nanoscale*, 2021, **13**, 17846–17853.

11 Y. Xie, J. Huang, R. Xu, D. He, M. Niu, X. Li, G. Xu, L. Cao and L. Feng, *Molecules*, 2022, **27**, 5961.

12 K. S. Bhat and H. S. Nagaraja, *Int. J. Hydrogen Energy*, 2019, **44**, 17878–17886.

13 S. Anantharaj, S. Kundu and S. Noda, *J. Mater. Chem. A*, 2020, **8**, 4174–4192.

14 H. Zhong, C. Campos-Roldán, Y. Zhao, S. Zhang, Y. Feng and N. Alonso-Vante, *Catalysts*, 2018, **8**, 559.

15 J. Lu, G. Qian, L. Luo, H. He and S. Yin, *Int. J. Hydrogen Energy*, 2021, **46**, 676–682.

16 H. Tian, X. Cui, L. Zeng, L. Su, Y. Song and J. Shi, *J. Mater. Chem. A*, 2019, **7**, 6285–6293.

17 S. Kajita, T. Eda, S. Feng, H. Tanaka, A. Bieberle-Hütter and N. Ohno, *Adv. Energy Sustain. Res.*, 2023, **2200141**, 2200141.

18 S. Suragtkhuu, S. Sunderiya, S. Purevdorj, M. Bat-Erdene, B. Sainbileg, M. Hayashi, A. S. R. Bati, J. G. Shapter, S. Davaasambuu and M. Batmunkh, *Nanoscale Adv.*, 2023, **5**, 349–355.

19 Y. L. Kim, H.-A. Choi, N.-S. Lee, B. Son, H. J. Kim, J. M. Baik, Y. Lee, C. Lee and M. H. Kim, *Phys. Chem. Chem. Phys.*, 2015, **17**, 7435–7442.

20 W. Wu, J. Yao, S. Liu, L. Zhao, L. Xu, Y. Sun, Y. Lou, J. Zhao, J.-H. Choi, L. Jiang, H. Wang and G. Zou, *Nanotechnology*, 2019, **30**, 355701.

21 A. Agrawal, S. H. Cho, O. Zandi, S. Ghosh, R. W. Johns and D. J. Milliron, *Chem. Rev.*, 2018, **118**, 3121–3207.

22 Y. Zhao, S. Wei, L. Xia, K. Pan, B. Zhang, H. Huang, Z. Dong, H.-H. Wu, J. Lin and H. Pang, *Chem. Eng. J.*, 2022, **430**, 133040.

23 H. Yu, J. Wang, X. Wang, N. Yu, X. Zuo, Y. Xue, N. Cai, J. Liu, J. Wang and F. Yu, *Sustainable Energy Fuels*, 2022, 74–83.

24 W. Yang and S. Chen, *Chem. Eng. J.*, 2020, **393**, 124726.

25 H. Sun, Z. Yan, F. Liu, W. Xu, F. Cheng and J. Chen, *Adv. Mater.*, 2020, **32**, 1806326.

26 Y. Zhang, K. Liu, F. Wang, T. A. Shifa, Y. Wen, F. Wang, K. Xu, Z. Wang, C. Jiang and J. He, *Nanoscale*, 2017, **9**, 5641–5647.

27 J. Gaidelene, A. Kuzmin, J. Purans and C. Guéry, *Phys. Status Solidi*, 2005, **2**, 149–152.

28 M. E. Schweinefuß, I. A. Baburin, C. A. Schröder, C. Näther, S. Leoni and M. Wiebcke, *Cryst. Growth Des.*, 2014, **14**, 4664–4673.

29 M. Balık, V. Bulut and I. Y. Erdogan, *Int. J. Hydrogen Energy*, 2019, **44**, 18744–18755.

30 J. Pandey, S. Mukherjee, D. Rawat, S. Athar, K. S. Rana, R. C. Mallik and A. Soni, *ACS Appl. Energy Mater.*, 2020, **3**, 2175–2181.

31 S. Mukherjee, R. Chetty, P. V. P. Madduri, A. K. Nayak, K. Wojciechowski, T. Ghosh, K. Chattopadhyay, S. Suwas and R. C. Mallik, *Dalton Trans.*, 2019, **48**, 1040–1050.

32 J. Purans, A. Kuzmin, E. Cazzanelli and G. Mariotto, *J. Phys.: Condens. Matter*, 2007, **19**, 226206.

33 Y. Zhao, D. Wu, T. Tang, C. Lyu, J. Li, S. Ji, C. Yuan, K. San Hui, C. Zha, K. N. Hui and H. Chen, *J. Mater. Chem. A*, 2022, **10**, 4015–4023.

34 D. Park, H. Ju, T. Oh and J. Kim, *CrystEngComm*, 2019, **21**, 1555–1563.

35 Q. Zhang, Z. Ti, Y. Zhu, Y. Zhang, Y. Cao, S. Li, M. Wang, D. Li, B. Zou, Y. Hou, P. Wang and G. Tang, *ACS Nano*, 2021, **15**, 19345–19356.

36 S. Suragtkhuu, S. Sunderiya, S. Purevdorj, M. Bat-Erdene, B. Sainbileg, M. Hayashi, A. S. R. Bati, J. G. Shapter, S. Davaasambuu and M. Batmunkh, *Nanoscale Adv.*, 2023, 0–6.

37 Y. Yuan and Y. Iwasawa, *J. Phys. Chem. B*, 2002, **106**, 4441–4449.

38 S. Kumar and C. Rath, *Phys. Status Solidi*, 2020, **217**, 1900756.

39 C. Wang, X. Cui, J. Liu, X. Zhou, X. Cheng, P. Sun, X. Hu, X. Li, J. Zheng and G. Lu, *ACS Sens.*, 2016, **1**, 131–136.

40 Y. Huang, Y. Yu, Y. Yu and B. Zhang, *Sol. RRL*, 2020, **4**, 2000037.

41 C. Wang, X. Cui, J. Liu, X. Zhou, X. Cheng, P. Sun, X. Hu, X. Li, J. Zheng and G. Lu, *ACS Sens.*, 2016, **1**, 131–136.

42 K. Zhu, F. Shi, X. Zhu and W. Yang, *Nano Energy*, 2020, **73**, 104761.

43 M. A. Pires, C. Israel, W. Iwamoto, R. R. Urbano, O. Agüero, I. Torriani, C. Rettori, P. G. Pagliuso, L. Walmsley, Z. Le, J. L. Cohn and S. B. Oseroff, *Phys. Rev. B: Condens. Matter Mater. Phys.*, 2006, **73**, 224404.

44 Y. Huang, Y. Yu, Y. Yu and B. Zhang, *Sol. RRL*, 2020, **4**, 2000037.